Proper Orthogonal Decomposition of Unsteady Aerodynamic Flows

T. Andrianne, J. Ligot and G. Dimitriadis
University of Liege
Department of Aerospace and Mechanical Engineering
Aeroelasticity and Experimental Aerodynamics Research Group
http://www.ltas-aea.ulg.ac.be/

Research Report SOUF-FNRS-QT09001

December 16, 2009

Abstract

This work constitutes the final report for a project funded by the Fonds de la Recherche Scientifique. The objective of the project was to acquire and install Partical Image Velocimetry (PIV) hardware in the University of Liege Wind Tunnel facility in order to carry out the Proper Orthogonal Decomposition (POD) of unsteady aerodynamic flows. The characteristics and installation of the PIV system are described in the present report. Furthermore, the application of POD analysis to three different visualized flow cases is detailed. The flow cases were: flow behind a circular cylinder and separated flow over a rectangular wing. In all cases, emphasis was given to the combination of unsteadiness caused by both boundary layer separation and movement of the wind tunnel model. It is shown that the decomposition of flowfields that combine these two sources of unsteadiness is possible and informative.

1 Introduction

The modal decomposition of unsteady flowfields was proposed in the 1990s by several authors, e.g. Hall [1] or Dowell et al [2]. Proper Orthogonal Decomposition (POD) is one method that can be used in order to perform this modal decomposition; it became popular for aerodynamics research in the 2000s, starting with Tang et al [3], although it was first proposed for use in fluid dynamics in the 1960s by Lumley [4].

The basic principle of POD is the creation of a mathematical model of an unsteady flow that decouples the spatial from the temporal variations. A 2D flowfield described by the horizontal velocity u(x,y,t) and the vertical flow velocity v(x,y,t) can thus be expressed as

$$u(x,y,t) \quad = \quad \bar{u}(x,y) + u'(x,y,t) = \bar{u}(x,y) + \sum_{i=1}^{M} q_i(t)\phi_{u,i}(x,y)$$

$$v(x,y,t) \quad = \quad \bar{v}(x,y) + v'(x,y,t) = \bar{v}(x,y) + \sum_{i=1}^{M} q_i(t)\phi_{v,i}(x,y) \tag{1}$$

where $\bar{u}(x,y)$ and $\bar{v}(x,y)$ are obtained by time averaging the flowfield over M time instances, while $u'(x,y,t)$ and $v'(x,y,t)$ are time-dependent fluctuations from the mean. These fluctuations are decomposed using M mode shapes $\phi_{u,i}(x,y)$, $\phi_{v,i}(x,y)$ and M generalized co-ordinates $q_i(t)$. For a reduced order model, the number of modes, $N << M$, is to be chosen as a compromise between model simplicity and model accuracy. The principle of the POD technique is to extract the most energetic modes that capture most of the unsteady flow energy.

The POD technique has been used to decompose several types of aerodynamic flows, such as the flow behind a disk [5], the flow past a delta wing [6], the unsteady flow impinging on an aircraft tail behind a delta wing [7], the unsteady flow around a F-16 fighter configuration [8] and others.

It should be noted that there are two types of POD research being carried out at the moment. The first concerns the decomposition of flowfields observed in experiments, on order to better understand the flow mechanisms and physics underlying these flows. The second type of research concerns the Reduced Order Modelling of unsteady Computational Fluid Dynamic (CFD) simulations or even, CFD/CSD (Computational Structural Dynamics) simulations, in order to produce simplified but representative models that can be used in, e.g. aircraft design.

The work of interest here is the first type, i.e. the experimental work. It is usually combined with high-speed Particle Image Velocimetry (PIV) measurements, although there are examples of other instrumentation being used, such as hot wire rakes [5]. The limitation of all work published on the subject is that the models around which the flowfield is measured are always static. Additionally, only one source of flow unsteadiness is ever considered.

The objective of the present work is to expand the methodology of the application of POD to experimental flowfields. There are two aspects to this expansion:

1. Allow the models to oscillate. The source of the unsteadiness will then be the movement of the model, as well as any unsteadiness due to flow separation.
2. Study the interaction between several different sources of unsteadiness. In particular observe how the modes generated at one region of the flowfield interact with modes generated at other regions.

2 Basics of Proper Orthogonal flow decomposition

Observation of an unsteady flow by PIV will, in general, yield M shapshots of a 2D section of the flowfield at times $t_1, \ldots, t_M$. These snapshots will, in general contain information on the $u(x,y,t)$ and $v(x,y,t)$ velocity vectors although other information can also be obtained (e.g. vorticity). The velocity vectors will be available on a spatial grid of size $n_y \times n_x$, i.e. there will be n_y gridpoints in the y direction with spacing δy and n_x in the x direction with spacing δx. Therefore, $u(x,y,t)$ and $v(x,y,t)$, will be available in discrete form, i.e. in the form of $n_y \times n_x \times M$ real arrays.

The time-averaged flow is represented by $(\bar{u}(x,y), \bar{v}(x,y))$, where

$$\begin{aligned}\bar{u}(x,y) &= \frac{1}{M}\sum_{i=1}^{M} u(x,y,t_i)\\ \bar{v}(x,y) &= \frac{1}{M}\sum_{i=1}^{M} v(x,y,t_i)\end{aligned}$$

and the unsteady velocity components are obtained simply from

$$\begin{aligned}u'(x,y,t) &= u(x,y,t) - \bar{u}(x,y)\\ v'(x,y,t) &= v(x,y,t) - \bar{v}(x,y)\end{aligned} \tag{2}$$

The Proper Orthogonal Decomposition procedure is then applied on the data matrix $\mathbf{C}$, the auto-correlation matrix of the total energy in the flow at every instance in time. For a continuous flow,

$$C(t_1,t_2) = \frac{1}{M}\int\int \left(u'(x,y,t_1)u'(x,y,t_2) + v'(x,y,t_1)v'(x,y,t_2)\right) dxdy \tag{3}$$

For a discrete flow, the integrals become summations. Using trapezoidal integration,

$$C_{i,j} = \frac{1}{M}\sum_{k=1}^{n_y-1} (G_{i,j,k} + G_{i,j,k+1})\delta y/2 \tag{4}$$

where $C_{i,j}$ is the element in the ith line and jth column of $\mathbf{C}$, $G_{i,j,k} = \sum_{l=1}^{n_x-1}(F_{i,j,k,l} + F_{i,j,k,l+1})\delta x/2$, $F_{i,j,k,l} = \left(u'_{k,l,i}u'_{k,l,j} + v'_{k,l,i}v'_{k,l,j}\right)$ and the notation $u'_{k,l,i}$ is shorthand for $u'(x_k, y_l, t_i)$. Higher order integration schemes can also be used.

The Proper Orthogonal Decomposition process requires the solution of the eigenvalue problem

$$\mathbf{CA} = \lambda\mathbf{A} \tag{5}$$

where $\mathbf{A}$ are the matrix of eigenvectors of the $\mathbf{C}$ matrix and λ are its eigenvalues. If the eigenvectors are normalized in the form $\mathbf{a}_i/\sqrt{\lambda_i M}$, where $\mathbf{a}_i$ is the ith column of $\mathbf{A}$, then they will form an orthonormal basis. The mode shapes $\phi_{u,i}$ and $\phi_{v,i}$ can be constructed from

$$\begin{aligned}\phi_{u,i}(x,y) &= \frac{1}{\sqrt{\lambda_i M}}\sum_{m=1}^{M} u'(x,y,t_m)a_{m,i}\\ \phi_{v,i}(x,y) &= \frac{1}{\sqrt{\lambda_i M}}\sum_{m=1}^{M} v'(x,y,t_m)a_{m,i}\end{aligned} \tag{6}$$

where $a_{m,i}$ is the mth element of the ith eigenvector of $\mathbf{C}$. The mode shapes are only functions of space but can be used to describe the unsteady flowfield when combined with the generalized coordinates $q_i(t)$, which can be obtained from

$$q_i(t) = \int\int \left(u'(x,y,t)\phi_{u,i}(x,y) + v'(x,y,t)\phi_{v,i}(x,y)\right) dxdy \tag{7}$$

or from the discrete version of this equation.

There are M eigenvalues and hence M sets of mode shapes and generalized coordinates. However, the aim of POD is to create a reduced order model, using only the first N modes that contain most of the fluctuating flow energy. To this end, the quantity $\lambda_i / \sum_{i=1}^{M} \lambda_i$ can be inspected, assuming that λ_i is ordered from highest to lowest eigenvalue. Kim et al [7] note that it should be $\sum_{i=1}^{M} \lambda_i = 1$, however this depends on the scaling used by the eigenvalue estimator, so looking at the ratio $\lambda_i / \sum_{i=1}^{M} \lambda_i$ is safer. If the first N eigenvalues are chosen, that have ratios higher than, say, 10% then a N mode model will be created.

Finally, the N-mode approximation of the complete velocity field can be reconstructed from the N retained modes using equation 1

$$\begin{aligned} u^*(x,y,t) &= \bar{u}(x,y) + \sum_{i=1}^{N} q_i(t)\phi_{u,i}(x,y) \\ v^*(x,y,t) &= \bar{v}(x,y) + \sum_{i=1}^{N} q_i(t)\phi_{v,i}(x,y) \end{aligned}$$

The POD procedure described above will be applied (with some modifications) to experimentally observed unsteady flows behind two different wind tunnel models: a circular cylinder and a rectangular wing.

3 PIV system characteristics

The PIV system used for these experiments consists of the following components:

1. A Litron LDY301-PIV Q-switched laser system. It is a dual power, dual cavity laser with a wavelength of 527nm, switching at 1000Hz. The two laser beams contain 2×10mJ of energy.
2. Optical modules for producing a laser sheet.
3. A Phantom V9.1 camera with a maximum resolution of 1600×1200 pixels at a frequency of 1KHz and 6GB of internal memory buffer.
4. A timer box for synchronizing the laser with the camera.
5. A seeding generator with 3 bar back pressure suitable for PIV particle generation.
6. Dantec Dynamics Studio PIV data acquisition and analysis software.
7. A high specification Personal Computer.

In practice, the system is capable of capturing PIV data in a window of around 13×11cm at a frequency of 1000Hz. Higher frequencies can be achieved for smaller windows.

4 PIV system installation

The laser system was installed on top of the Aeronautical working section of the ULg wind tunnel. The roof of the tunnel features a large perspex window, through which the laser sheet is projected downwards. The laser is installed on a 2 degree-of-freedom mechanized positioning system, activated by two Charlyrobot digitally

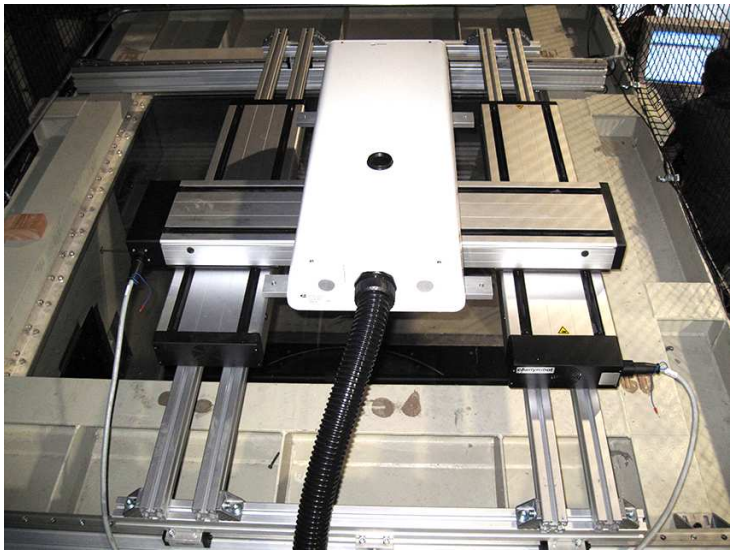

Figure 1: Laser installation on top of the ULg wind tunnel

controlled units. The setup allows the coverage of most of the working section by the laser sheet. Figure 1 depicts the laser installed on the roof of the wind tunnel, with its mechanized positioning system.

Figure 2: Camera installation on the side of the working section

The camera is installed on the side of the wind tunnel's Aeronautical section, looking through a perspex window. It is mounted on a rigid beam by means of a swivel joint, as seen in figure 2. The height of the camera can be adjusted by moving manually the beam upwards or downwards. A more sophisticated camera motion system is under development.

The particle generator is placed inside the wind tunnel, secured on the turning vanes of the first corner aft of the working section. The generation is turned on and the wind tunnel is operated in close return mode. When enough particles are

present in the flow, the generation is turned off and the seeding generator removed from the wind tunnel so as not to disturb the airflow.

5 Flow behind a circular cylinder

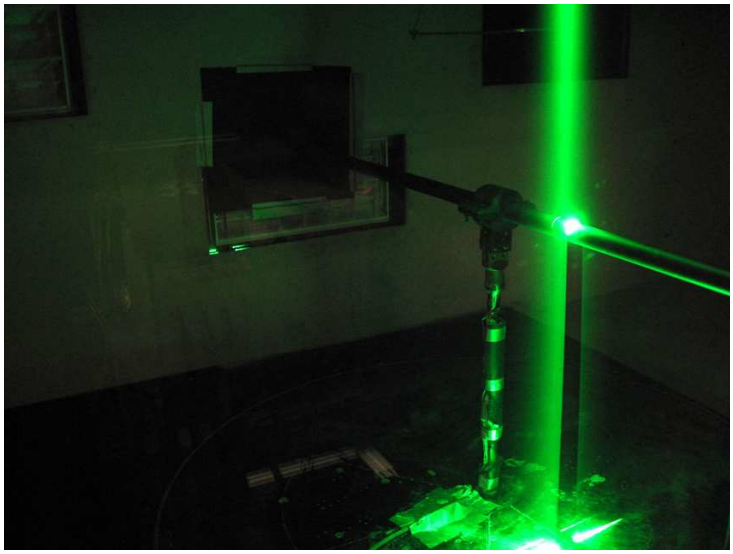

Figure 3: Laser sheet illuminating 2D section of flow around a cylinder

A circular cylinder of 36mm diameter and 1.32m span was placed in the wind tunnel, supported by its mid-span point near the middle of the Aeronautical working section. The cylinder was made of aluminium tube and painted matt black. The laser sheet was placed on the side of the cylinder nearest to the working section's observation window and aligned with the airflow, so as to illuminate a 2D section of flow around the cylinder. The laser sheet position can be seen in figure 3. Notice that the centre of the laser sheet lies aft of the cylinder. The very sharp shadow under the cylinder is also worth noting.

The cylinder is rigidly supported but is flexible itself. Its first symmetric bending mode has a frequency of around 80Hz. Therefore, it is expected that when the frequency of the Von Karman vortex street behind the cylinder matches the first bending frequency, the illuminated section of the cylinder will oscillate quite visibly. This setup is ideal for the purposes of the present investigation, as it allows the examination of the unsteady flow behind both a static and a vibrating object.

5.1 PIV results

Figure 4 shows a snapshot of the illuminated particles around the cylinder. It can be seen that the laser illuminates the aft upper section of the cylinder itself (white arc) as well as seeded particles on the upper surface of the cylinder and in the wake. Evidently, there are no illuminated particles in the shaded area under the cylinder.

The PIV system takes two such photos at a very short time interval, typically $1 - 1000\mu$s. These images are divided into subregions (e.g. 64×64 or 128×128 regions) and each region of the first photo is correlated to each region of the second photo. The aim of the analysis is to decided where each region of photo 1 has

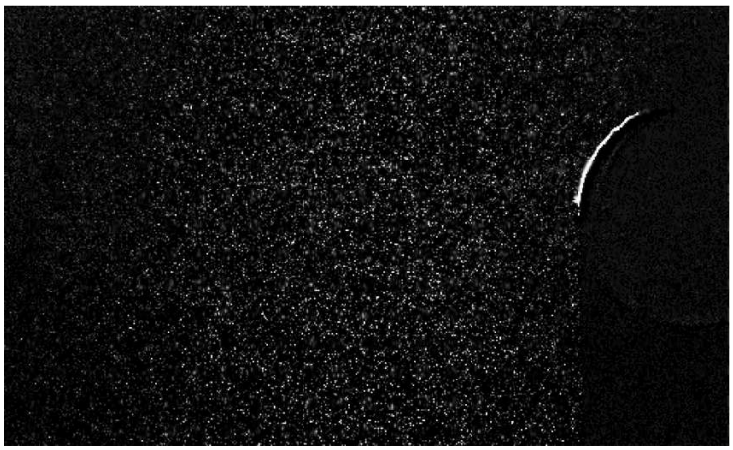

Figure 4: Illuminated particles around the cylinder

moved to on photo 2. Thus, a velocity vector is placed in the centre of each region. The entire process is carried out by means of the Dynamics Studio PIV software and requires calibration by means of the free stream airspeed and a characteristic length, in this case the cylinder diameter.

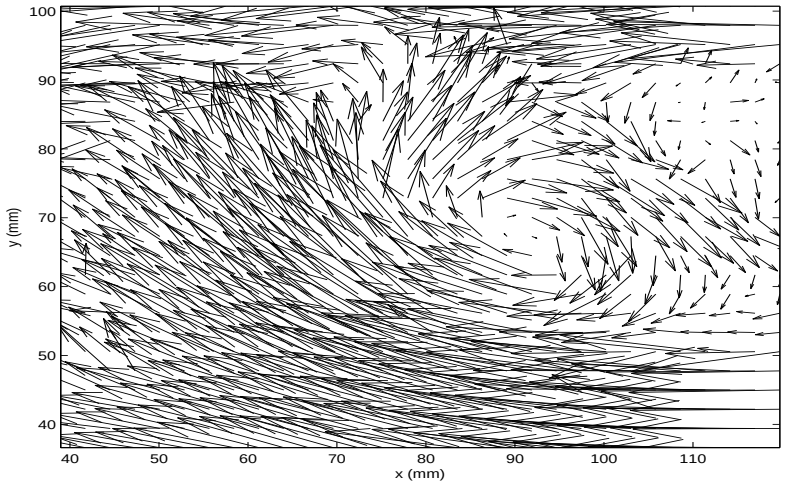

Figure 5: Computed velocity vectors on a sample snapshot

The end result of the PIV data reduction process is a vector field calculated at each instance in time for which the visualization took place, as shown in figure 5. The image correlation process can sometimes lead to the calculation of bad vectors; these are detected and replaced by averages of all the neighboring vectors.

PIV visualizations for the circular cylinder were carried out at airspeeds from 10 to 20m/s, at a sampling frequency of 1000Hz and a sampling times from 0.1s to 0.5s. The recovered unsteady vector fields had a resolution of 24 gridpoints in the y-direction and 41 in the x-direction. Therefore, the sizes of the u and v matrices ranged from $24 \times 41 \times 100$ to $24 \times 41 \times 500$.

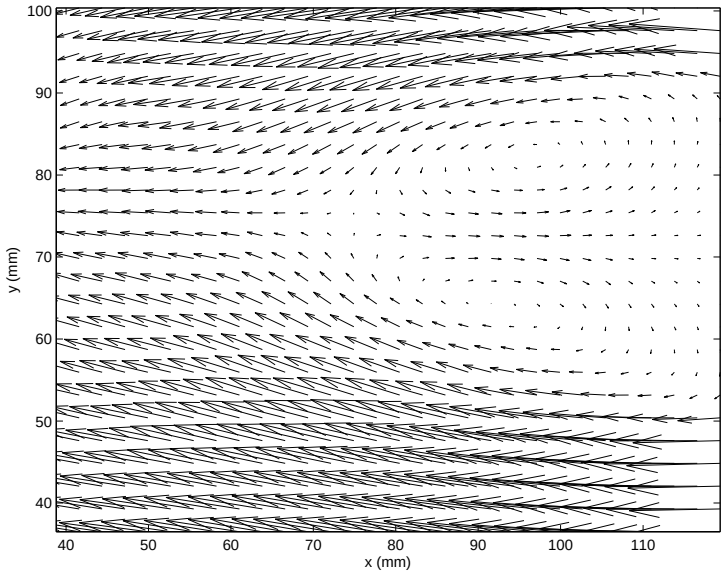

Figure 6: Mean flow vectors for test 1

5.2 POD analysis

At the end of the PIV data treatment, a set of $u(x, y, t)$ and $v(x, y, t)$ matrices were obtained for each tested airspeed. These matrices where then analyzed using the POD procedure described in section 2. Sample results from three airspeeds are presented and discussed in this section. These are labeled as:

- Test 1: Free stream airspeed of 18.8m/s, sampling frequency of 1000Hz, sampling time of 0.298s, PIV laser sheet at 0.2m from the cylinder's midpoint.
- Test 2: Free stream airspeed of 13m/s, sampling frequency of 1000Hz, sampling time of 0.099s, PIV laser sheet at 0.2m from the cylinder's midpoint.
- Test 3: Free stream airspeed of 13.9m/s, sampling frequency of 1000Hz, sampling time of 0.099s, PIV laser sheet at 0.2m from the cylinder's midpoint.
- Test 4: Free stream airspeed of 14.8m/s, sampling frequency of 1000Hz, sampling time of 0.099s, PIV laser sheet at 0.4m from the cylinder's midpoint

The Reynolds numbers for the three tests range from 40,000 to 55,000, which puts the flowfield in the 'transitional in the shear layer' category. In other words, the boundary layer on the cylinder's surface is expected to be laminar. After separation, there is periodic ejection of vortices in the wake, as in the case of laminar vortex shedding, but the shear layer causing this ejection is transitional, giving rise to small turbulent eddies.

Test 1 is used as the reference test, as it lies very far from aero-structural resonance and, therefore, there is negligible cylinder movement. Test 3 lies right on resonance and the cylinder vibrates significantly at the PIV measurement position. For all the tests, the first step in the POD procedure was to define the region of interest, so as not to include in the POD calculations the velocity vectors under the cylinder, which are not valid. The region of interest was therefore limited to a point just downstream of the cylinder.

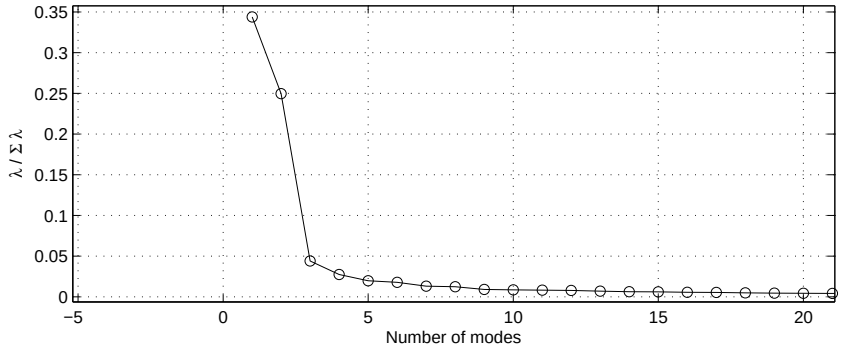

Figure 7: Eigenvalue ratios for the first 20 eigenvalues for test 1

5.2.1 Test 1

The next step in the POD procedure for Test 1 was to calculated the mean flow. This calculation involved the time averaging of the $u(x, y, t)$ and $v(x, y, t)$ matrices, leading to the mean flow shown in figure 6. It can be seen that the mean flow is essentially an area of slow, recirculating flow, located just behind the cylinder. In other words, it can be seen as the steady wake, to which an unsteady wake is superimposed.

Once the mean flow was subtracted from $u(x, y, t)$ and $v(x, y, t)$ the unsteady vector fields $u'(x, y, t)$ and $v'(x, y, t)$ were obtained and Proper Orthogonal Decomposition was applied. The eigenvalue ratios $\lambda_i / \sum_{i=1}^{M} \lambda_i$ obtained for the first 20 modes are shown in figure 7. It can be seen that only the first two eigenvalues have significant contributions to the total energy in the unsteady flow, of 35% and 25% respectively. All higher eigenvalues have contributions of less than 5% and can therefore be neglected.

The mode shapes associated to the two retained eigenvalues are shown in figure 8, plotted as filled contour plots. Subfigure 8(a) shows plots the values of $\phi_u(x, y)$ (left) and $\phi_v(x, y)$ (right) for mode 1 as colours, blue signifying a low value and red signifying a high value. Subfigure 8(b) depicts the same information for mode 2. The horizontal distance between a maximum and a minimum grows from 30mm to 40mm with distance downstream. The vertical distance increases with downstream distance from 30mm to 46mm. If the mode shapes are assumed to be periodic, i.e. repeatable further downstream, then the two modes are separated by 1/4 of a period. It should be noted that the distances between maxima and minima are not constant because the measurement is just behind the cylinder, where there are large variations in the mean flow, as seen in figure 6. It is likely that the distances between maxima and minima are stabilized further downstream.

Figure 9 shows the variation in time of the two retained generalized coordinates. It can be seen that the two generalized coordinates have the same fundamental frequency of 107.5Hz. Furthermore, they are both subjected to a beating phenomenon, with the response amplitudes dropping momentarily at around 0.12s and again at around 0.3s. This beating demonstrates that the flow is quasi-periodic, with significant variations in amplitude occurring momentarily. This quasi-periodic nature is justified by the fact that the flow is transitional in the shear layer and there are small turbulent eddies absorbing some of the flow energy.

In fact, the two mode shapes of figure 8 are the dominant modes and can be viewed as 'laminar' modes. The modes that have been neglected can be viewed as

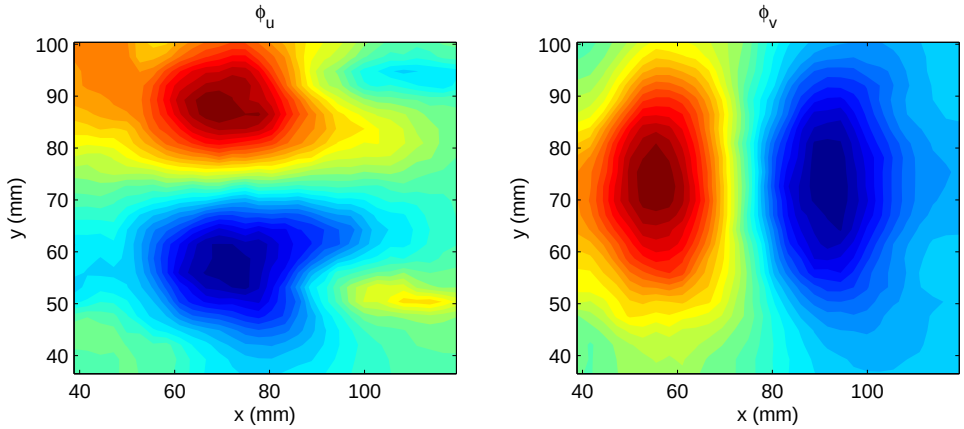

(a) Mode 1

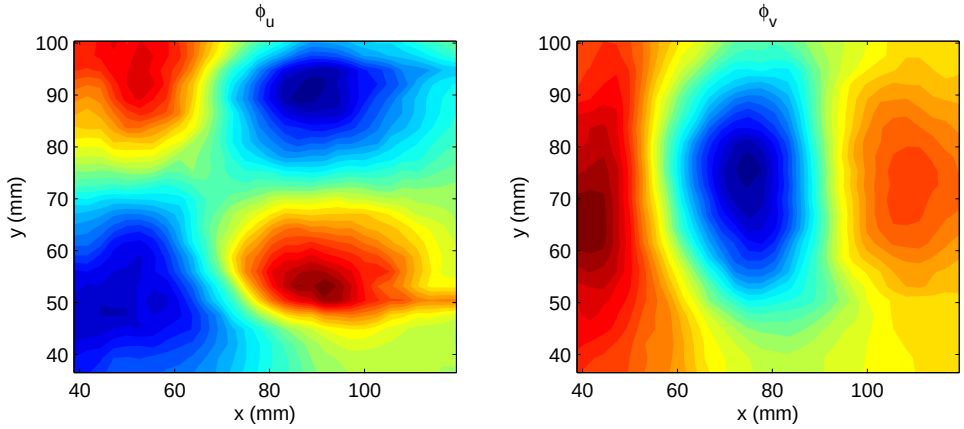

(b) Mode 2

Figure 8: The first two mode shapes for test 1

'turbulent' modes, which contain little energy over the complete time history but can momentarily absorb energy from the dominant modes. This is exactly what happens in the case of this test. At time indices of 0.12s and 0.3s, the response amplitude of modes 1 and 2 drops significantly; simultaneously the response amplitude of mode 3 increases visibly, as shown in figure 10(a), which plots the variation of generalized coordinate $q_3(t)$ with time. It can be clearly seen that the maxima of this mode occur at 0.12s and 0.3s.

The mode shape for mode 3 can be seen in figure 10(b). It is clear that this mode shape is significantly noisier than the mode shapes of the first two modes, shown in figure 8. This noisiness is consistent with the hypothesis that mode 3 represents turbulent flow energy. It should be mentioned that higher modes do not demonstrate any clear increases in amplitude at 0.12s and 0.3s. Therefore, a complete model of the flow of Test 1 will contain:

- two modes if only the laminar flow is of interest
- three modes if it is desired to account for some of the energy momentarily lost by the laminar modes

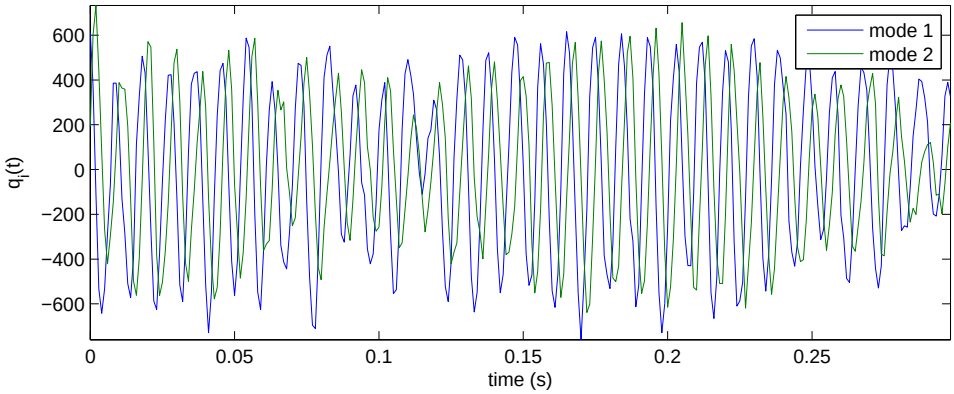

Figure 9: Variation in time of the two retained generalized coordinates, Test 1

5.2.2 Test 2

Test 2 is similar to Test in the sense that resonance is not occurring yet; however, the condition is much closer to resonance than Test 1 and the amplitude of vibration of the cylinder is small but noticeable. Under these circumstances, the effect of evaluating a mean flow and subtracting it from the total vector field must evaluated. In effect, as the mean flow is the steady wake behind the cylinder, if the cylinder oscillates by a significant amount, then the concept of a steady wake is no longer valid and the mean flow should not be evaluated. In other words, while it is still possible to calculate values for $\bar{u}$ and $\bar{v}$ over the entire time history, these values will not be the same over a different time history. In essence, the movement of the cylinder is an excitation force that is applied to fluid; it will respond at the excitation frequency and at higher harmonics but there will be no response component with zero frequency.

Nevertheless, if the amplitude of oscillation is very small, then evaluating and subtracting the mean flow will not cause big errors in the POD procedure. For Test 2, the POD method was applied twice, the first time after subtracting the mean flow and the second after subtracting only the wind tunnel free stream, U. In other words, in the first application the POD analysis was carried out on u' and v' using equations 3 to 7 while in the second it was carried out on $u - U$ and v, such that

$$C(t_1, t_2) = \frac{1}{M} \int\int \left((u(x, y, t_1) - U)(u(x, y, t_2) - U) + v(x, y, t_1)v(x, y, t_2) \right) dxdy \tag{8}$$

with

$$\phi_{u,i}(x, y) = \frac{1}{\sqrt{\lambda_i M}} \sum_{m=1}^{M} (u(x, y, t_m) - U)a_{m,i}$$
$$\phi_{v,i}(x, y) = \frac{1}{\sqrt{\lambda_i M}} \sum_{m=1}^{M} v(x, y, t_m)a_{m,i} \tag{9}$$

and

$$q_i(t) = \int\int \left((u(x, y, t) - U)\phi_{u,i}(x, y) + v(x, y, t)\phi_{v,i}(x, y) \right) dxdy \tag{10}$$

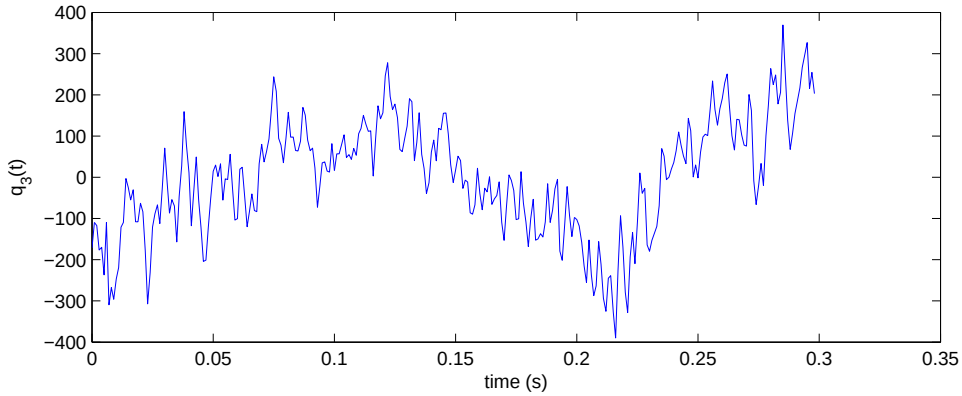

(a) $q_3(t)$

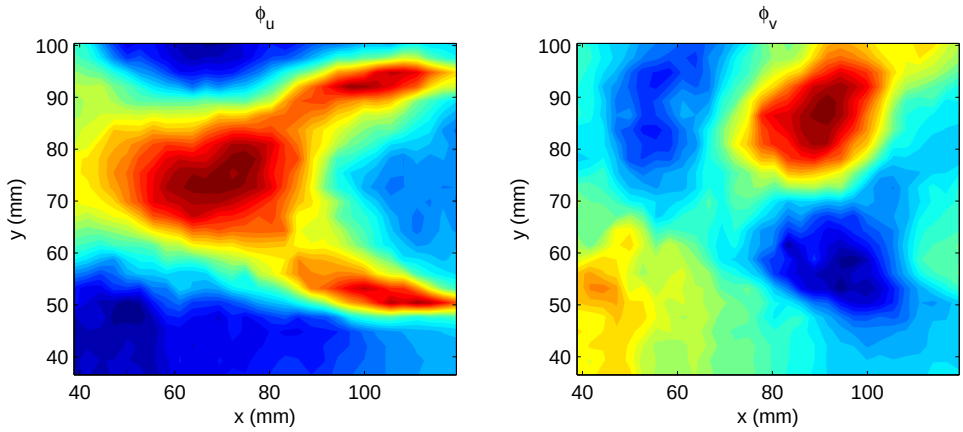

(b) Mode 3

Figure 10: The third mode for test 1

For the first application, the number of retained modes was 2, i.e. only the laminar unsteady flow modes were found to be significant. For the second application, the number of retained modes was 3. The first mode represented the mean flow while the other two modes represented the laminar unsteady flow and were very similar to the modes of the first application and of figure 8 (obtained for Test 1). It is interesting to compare the mean flow subtracted from the data in the first application to the first mode obtained from the second application. Figure 11 shows contour plots of the first mode $\phi_{u,1}$ and $\phi_{u,2}$ evaluated from the application of POD to $u - U$ and v (top two plots) and of the mean flow components $\bar{u}$ and $\bar{v}$ (bottom plots). It can be seen that the two sets of contour plots are very similar. Therefore, the POD procedure described by equations 8 to 10 will calculate the mean flow as the most energetic mode.

This is quite an interesting result because it suggests that there is no need to subtract the mean flow. If there is a steady component to the flow, then it will be identified automatically as the first mode. If there is no steady component then equations 8 to 10 should be used anyway. Figure 12 shows the time response of the three resulting generalized coordinates. It can be seen that the generalized coordinate of the first mode is nearly constant with a value of around 1450, while the coordinates of the other two modes oscillate around zero. It is clear that the POD procedure can differentiate between steady and unsteady responses.

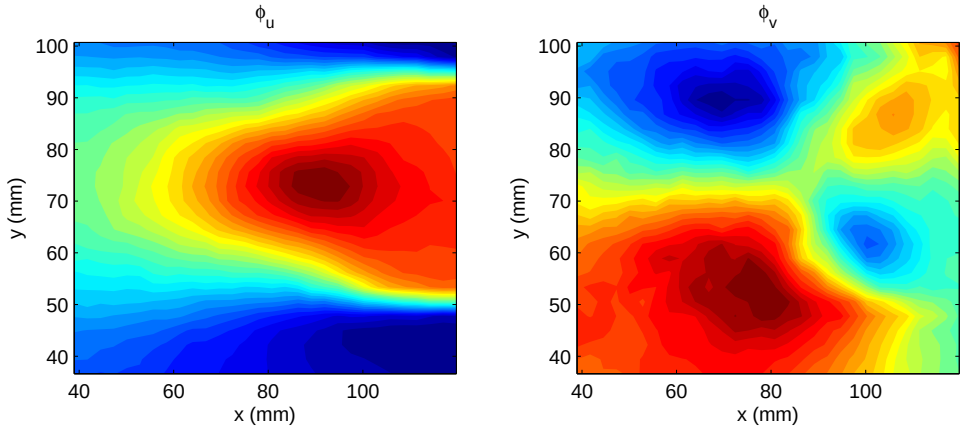

(a) Mode 1

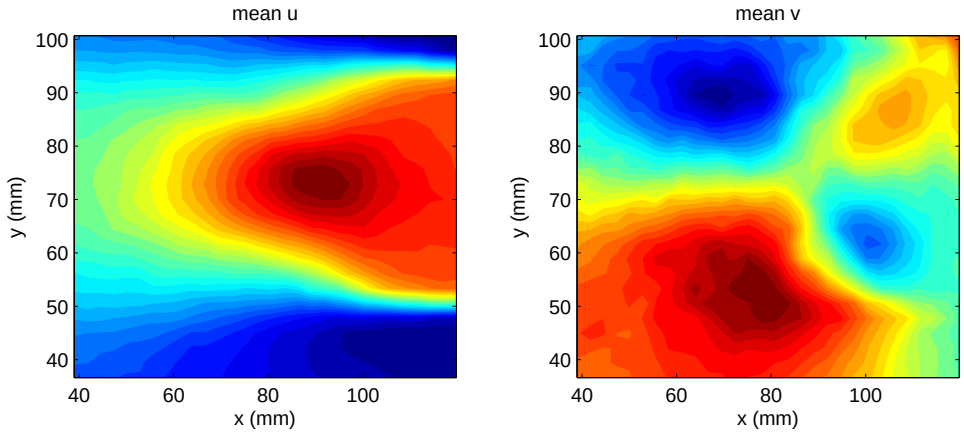

(b) Mean flow

Figure 11: The first mode shape for test 2 (top) compared to the mean flow (bottom)

5.2.3 Test 3

For Test 3 the POD procedure was carried out only using equations 8 to 10. As mentioned before, Test 3 gave rise to significant amplitudes of cylinder vibration as the flow frequency was very close to a natural frequency of the cylinder. Again, three modes were retained, one representing a mean flow and two representing the laminar oscillating flow.

The response amplitudes of the three generalized coordinates were significantly higher than in the case of Test 2, as seen in figure 13. Even the generalized coordinate of mode 1 is far more unsteady, although its variation in time is not periodic. This aperiodic variation suggests that there is a component of the cylinder vibration in the flow data but it is of the same order as the turbulent disturbances and/or experimental error. This was indeed the case, as the measurement point was close to the cylinder's midpoint (see figure 3), therefore the local vibration amplitude was small, of the order of 1mm.

5.2.4 Test 4

The final test was carried out at a slightly higher airspeed but, crucially, the PIV laser sheet was positioned at a span-wise point further from the cylinder's midpoint

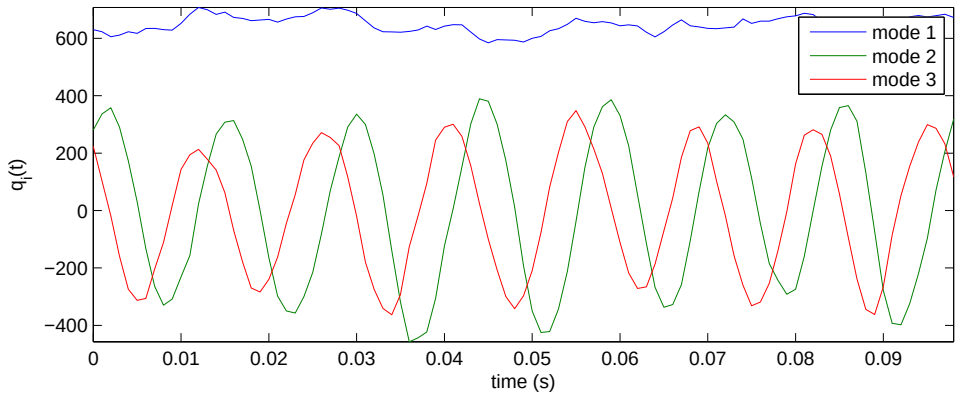

Figure 12: Variation in time of the three retained generalized coordinates, Test 2

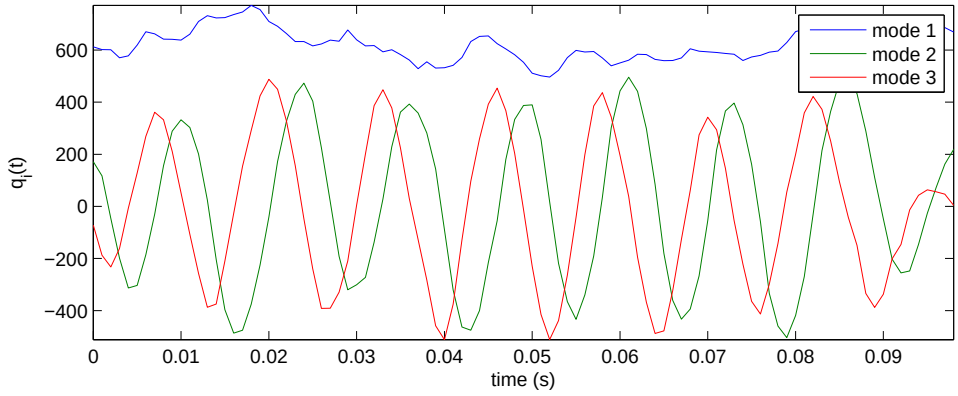

Figure 13: Variation in time of the three retained generalized coordinates, Test 3

than for the other three tests. The resulting mode shapes were similar to those obtained during Test 3 but noisier. The resulting generalized coordinates are plotted on figure 14. It can be clearly seen that the amplitude of the response of the first generalized coordinate is now much higher than in the case of figure 13. Furthermore, despite the randomness of this response, there is a clear periodic component at a frequency close to that of the oscillating modes.

The conclusions from Test 4 suggest that POD can decompose flowfields that feature unsteadiness due to the presence of both separated flow and structural motion of the wind tunnel model. However, for this decomposition to be successful, the response amplitude of the structure must be significantly higher than the size of the turbulent eddies.

5.2.5 Mode shapes variation with airspeed

Here, the variation of the modes shapes with airspeed will be discussed. Only the free stream is subtracted from the local velocity field for the results in this subsection, not the mean flow. It was observed that the first three modes, i.e. the steady flow and the two laminar modes, change very little in shape with airspeed.

Figure 15 shows vector plots of the first three modes. Mode one (figure 15(a)) consists of two areas of recirculation behind the top and the bottom of the cylinder.

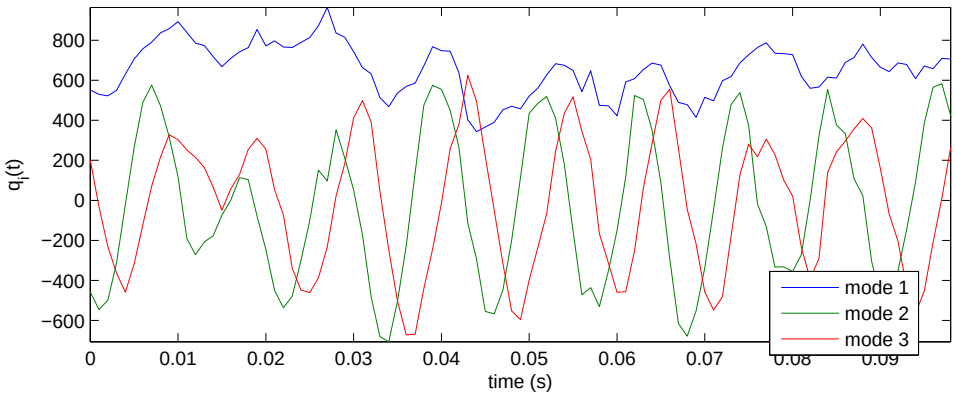

Figure 14: Variation in time of the three retained generalized coordinates, Test 4

Between them, they cause a significant are of flow towards the cylinder with a height approximately equal to the cylinder's diameter. Mode two (figure 15(b)) consists of a large vortex, positioned approximately one diameter behind the cylinder and centered on the cylinder's centerline. It is accompanied by two much smaller areas of recirculation lying just behind the top and bottom of the cylinder. Mode 3 (figure 15(c)) consists of two counter-rotation vortices at approximately half a diameter (the strongest) and one diameter (the weakest) behind the cylinder. They are both lying on the cylinder's centerline. As mentioned above, these three modes remain largely unaffected by the airspeed.

Figure 16 shows vector plots of mode 4 obtained for the four different tests, i.e. at four different airspeeds. It can be seen that all mode shapes are different. The mode shape for Test 1consists of four vortices; for Test 2 of three vortices, one of which is very week; for Test 3 the mode shape consists of three vortices again but in a different arrangement; finally, for Test 4 the number of vortices is difficult to determine because they are quite week and small.

The reason for the change in mode shape 4 with test airspeed may be numerical rather than physical. In fact, mode shapes very similar to that of figure 16(a) appeared as mode 6 in Test 3 and mode 5 in Test 4. Therefore, the mode shape can be preserved but its relative importance changes between tests. This phenomenon may provide justification for the assertion presented here concerning the higher modes, i.e. that modes higher than 3 represent transitional effects.

5.2.6 Flow frequency variation with airspeed

In order to verify that the PIV system and POD decomposition analysis are performing correctly, a large number of PIV measurements were carried out at airspeeds between 4m/s and 26m/s. The flow frequencies recovered by the POD method for all these measurements were then compared to the theoretical frequencies, assuming that the cylinder has a Strouhal number of 0.2 This comparison can be seen in figure 17, where the experimentally estimated frequencies are plotted as stars with error bars and the theoretical frequency is plotted as a green line. The error bars represent the frequency increment, equal to the sampling frequency divided by the number of time measurements M and is equal to 2.02Hz.

Figure 17 shows that the frequencies estimated from the decomposed PIV measurements are in good agreement with the theoretical predictions. It can be con-

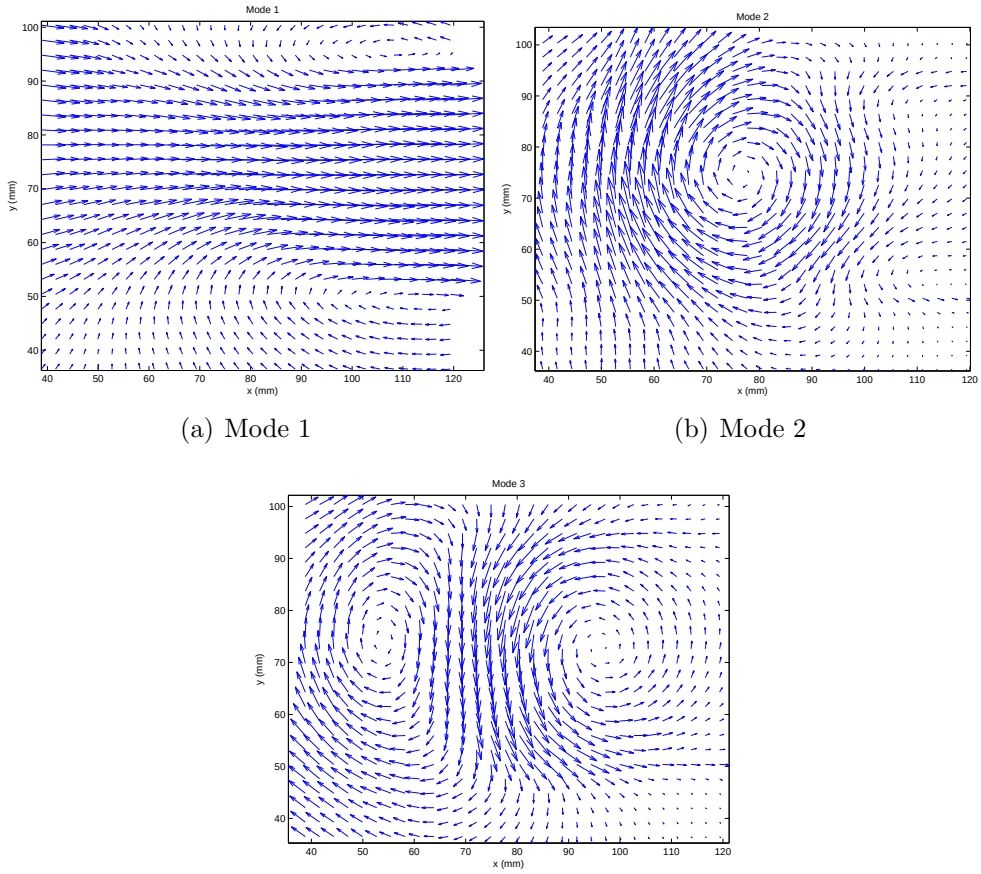

(a) Mode 1

(b) Mode 2

(c) Mode 3

Figure 15: Vector plots of the first three mode shapes

cluded that both the instrumentation and the POD analysis were correctly operated. The two dotted lines in the figure represent the airspeed limits at which significant cylinder vibration amplitudes were observed. Indeed, the first bending natural frequency of the cylinder is 78Hz and resonance phenomena were observed at airspeeds between 13.5m/s and 18m/s, corresponding to flow frequencies of 70-105Hz. The lock-in phenomenon, whereby the flow frequency adapts itself to the structure's natural frequency throughout the resonance airspeed range, is not evident in this data. The reason for this absence of lock-in is that the measurements used for constructing figure 17 were taken close to the cylinder's midpoint, as seen in figure 3, hence the vibration amplitudes were small.

6 Flow over a rectangular wing

A small aspect ratio rectangular wing with a chord of 30cm, span of 40cm and a NACA2412 profile was installed in the in the wind tunnel, supported by its mid-span point near the middle of the Aeronautical working section. The wing was made of plastic sheet and foam and painted matt black. The laser sheet was placed near the mid-span position of the wing and aligned with the airflow, so as to illuminate a 2D section of flow over the wing's upper surface. The laser sheet position can be seen in figure 18. Notice that the width of the laser sheet is smaller than the wing's chord.

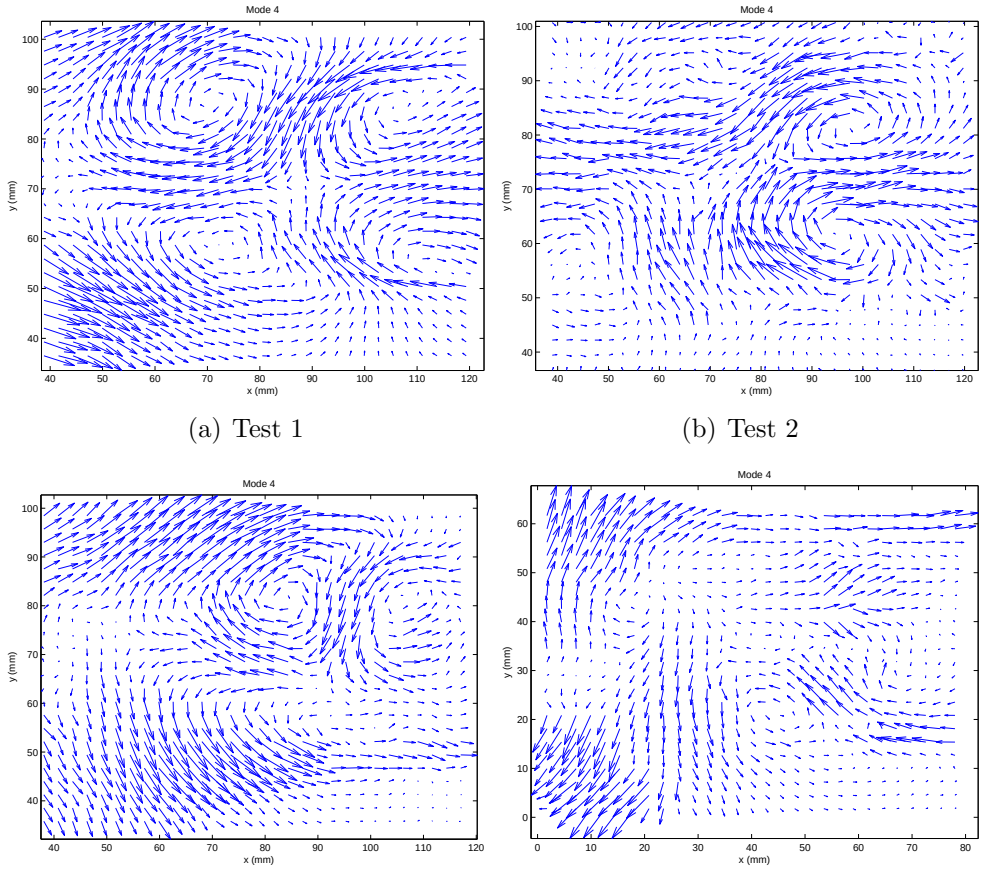

(a) Test 1 (b) Test 2

(c) Test 3 (d) Test 4

Figure 16: Vector plots of the fourth mode shape for the four different tests

The objective of the tests was to observe the separated flow on the upper surface of the wing. Two different positions were chosen for the visualization: the mid-chord point and the leading edge. The angles of attack considered ranged from 15 to 35 degrees. It was quickly determined that the leading edge visualizations did not yield any interesting unsteady behaviour; either the flow was attached, or completely separated with a stable shear layer and nearly stagnant flow behind it. Therefore, only results from the mid-chord visualizations will be presented in this report. In particular, three test cases will be described in detail:

- Test 1: Angle of attack of 16.2^o.
- Test 2: Angle of attack of 16.9^o.
- Test 3: Angle of attack of 23.2^o.

All test were carried out a a free stream airspeed of 12.8m/s, sampling frequency of 1000Hz, sampling time of 0.298s, and the laser sheet was centered on the mid-span/mid-chord point of the wing.

6.1 PIV results

Sample snapshots of the PIV visualizations for the three tests are presented in this section. Figure 19 shows a snapshot taken from the visualization of Test 1, at 16.2^o. The intermittent white/grey streak denotes the wing's surface, illuminated

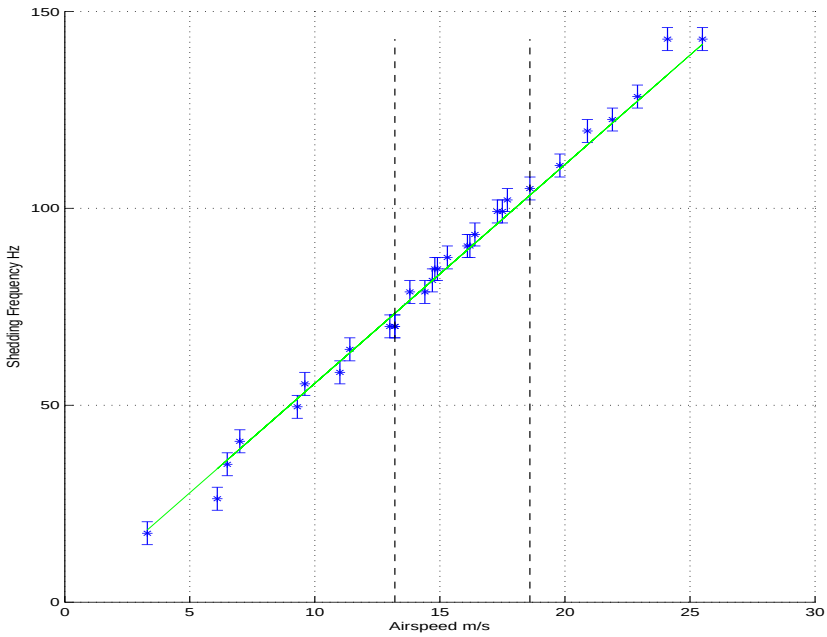

Figure 17: Comparison of estimated frequencies to theoretical frequencies

by the laser sheet. The yellow arrows are the local velocity vectors. Any arrows drawn by the PIV software under the wing's surface are invalid. It can be seen that the flow appears to be parallel to the wing's surface throughout the image. The image suggests that the flow is completely attached but, in fact, a study of all 298 snapshots reveals that there are perturbations on the wing's surface near the left edge of the image. These perturbations are small vortical structures that travel downstream at irregular time intervals.

Figure 20 shows a snapshot from the visualization of Test 2, at 16.9^o. In this case, there is a large vortical structure near the surface, which effectively reverses the flow. At the edge of the vortical structure, near the top of the image, the flow moves in the same direction as the free stream. Other snapshots from the same test contain more than one vortical structures and show that these structures propagate downstream.

Finally, figure 21 shows a snapshot from the visualization of Test 3, at 23.2^o. Here, the entire image contains reversed flow and some vortical structures can be observed. The complete visualization shows that some of these vortical structures travel upstream for a while before being lifted upwards and disappearing of the upper edge of the image.

The PIV results clearly shows that the flow is mostly attached on the wing's upper surface for Test 1, while it is separated for Tests 2 and 3. However, the separation mechanism has not been made evident yet. This can be achieved by mans of a POD analysis.

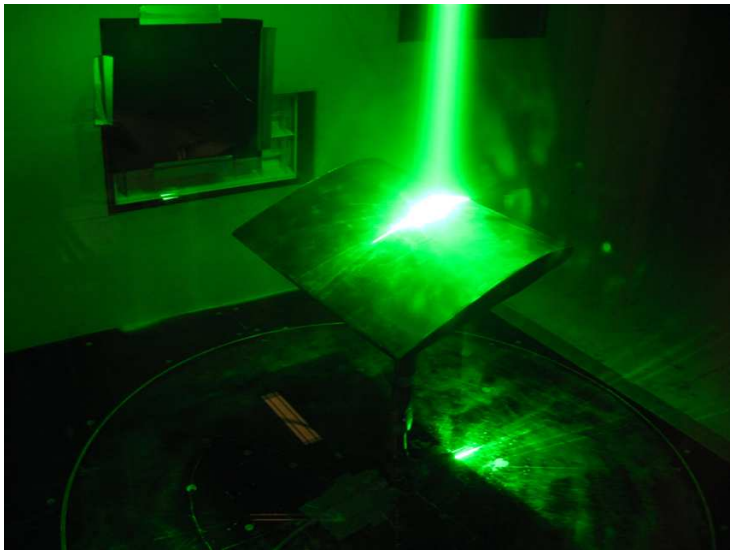

Figure 18: Laser sheet illuminating 2D section of flow over a rectangular wing

6.2 POD Results

Proper Orthogonal Decomposition was applied to all three test cases in order to attempt to explain the velocity fields observed by the PIV procedure. The rectangular wing was rigid and solidly attached at its mid-span point from the lower surface. It did not vibrate at measurable amplitudes during any of the wind tunnel tests. Therefore, the POD analysis was applied after subtracting the mean flow, i.e. using equations 2 to 7.

6.2.1 Test 1

Test 1 was, in a sense, the most interesting result obtained from the PIV measurements. While the flow seems attached everywhere, there are small perturbations that appear near the left edge of the image and move downstream at irregular intervals. Figure 22 shows the first four modeshapes calculated from the application of the POD procedure.

The first mode suggests that there is a recirculation area near left edge of the image, very close to the wing's surface. The other three modes show that there are perturbations throughout the illuminated area near the surface. Mode 1 could be proof that the flow separates for the first time in the vicinity of the recirculation area, but the other three modes, if taken to be valid, suggest that there is flow separation everywhere in the observed region.

Figure 23 shows the eigenvalue ratio $\lambda_i / \sum_{i=1}^{M} \lambda_i$ for the first 20 eigenvalues. It can be seen that, while the first mode contains nearly 35% of the unsteady flow energy, the other modes represent less than 5% of the flow energy each. It can be logically concluded that only mode 1 should be included in a POD model of the flow of Test 1. The other modes represent either small turbulent perturbations or errors in the calculation of the velocity field.

Making these hypotheses, it can be concluded that for Test 1 the flow is attached almost everywhere but separates in a region starting at around 70% of the chord. Therefore, the wing undergoes a trailing edge separation phenomenon at this airspeed. As the chord of the wing is larger than the width of the laser sheet, it is

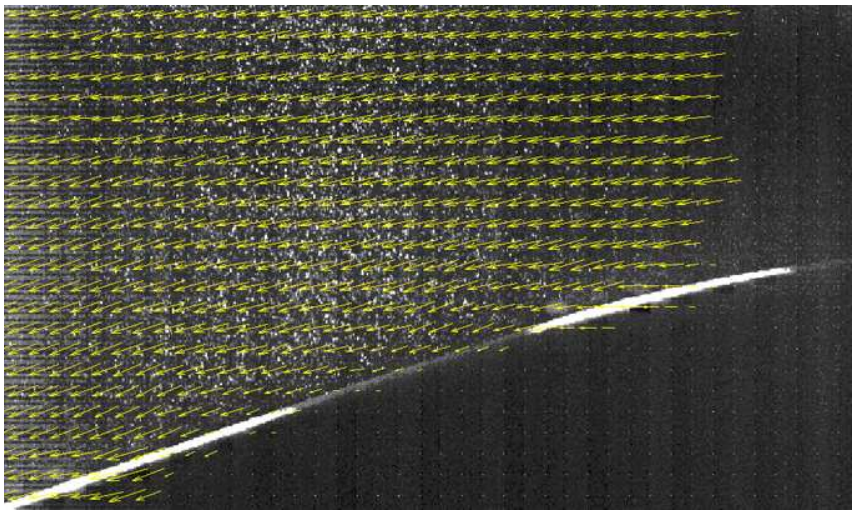

Figure 19: Sample snapshot of PIV visualizations for Test 1

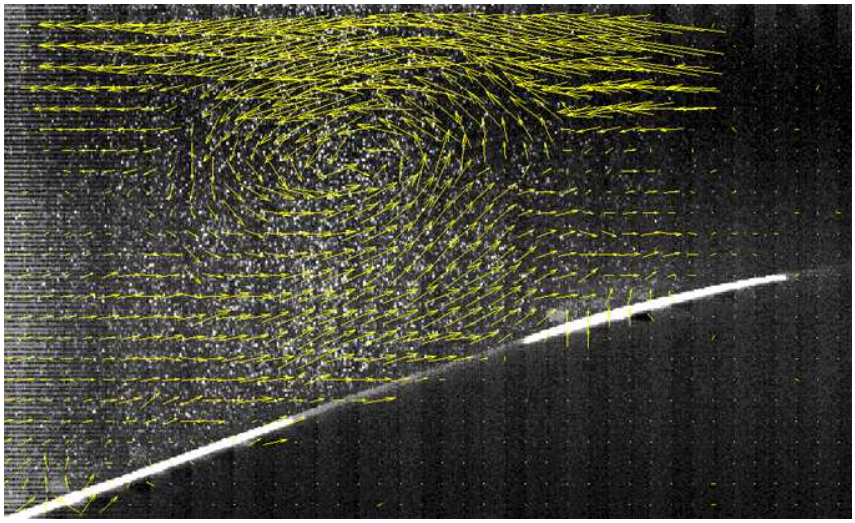

Figure 20: Sample snapshot of PIV visualizations for Test 2

not possible to visualize the rest of the separated flow without moving the camera and the laser. Such tests will be conducted in the future to verify the trailing edge separation hypothesis.

6.2.2 Test 2

Figure 24 shows the first four modeshapes calculated from the application of the POD procedure to the Test 2 vector fields. Mode 1 is a single vortex inducing significant recirculation velocities away from the surface but not affecting the local velocities near the surface. Mode 2 is a complex interaction of probably three vortices. Mode 3 comprises two counter-rotating vortices. Finally, mode 4 is similar to mode 2 only the direction of the largest vortex is reversed and its position slightly different.

Looking at the unsteady flow energy represented by the modes, it transpires that the first four modes all contain more than 5% of the energy. The first mode

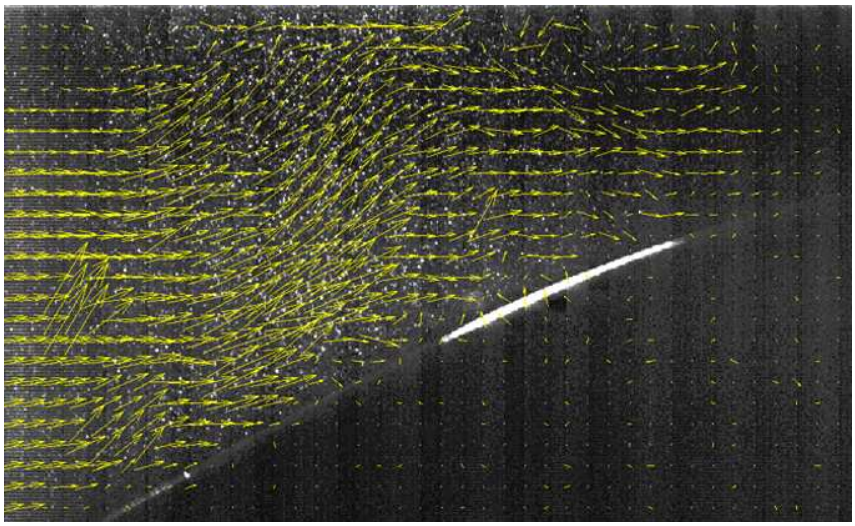

Figure 21: Sample snapshot of PIV visualizations for Test 3

represents around 21% while the other three represent 10%, 7% and 6% respectively. Therefore, a 4-mode POD model appears to be a good choice for the flow of Test 2. Figure 25 shows the variation in time of the four respective generalized coordinates. It is interesting to note that all four have very similar amplitudes and quite a random character. Their time responses are completely different to those observed during the cylinder experiment, see e.g. figure 9. Therefore, the flow separation observed in the wing experiment is much less ordered than the vortex ejection mechanism characterizing the cylinder. It is also interesting to note that mode 1 appears to be a lower frequency phenomenon compared to the other three modes.

6.2.3 Test 3

Figure 26 shows the first four modeshapes calculated from the application of the POD procedure to the Test 3 vector fields. Mode 1 is a single vortex centered near the top left corner of the image, inducing significant recirculation below it but not affecting the local velocities very near the surface. Mode 2 is a complex interaction of probably three vortices but only one of them is visible in the image. Mode 3 is a very weak effect, only significant near the left edge of the image. Finally, mode 4 is similar to mode 2 only the direction of the circulation has been reversed.

Looking at the unsteady flow energy represented by the modes, it transpires that the first three modes all contain more than 5% of the energy. The first mode represents around 21% while the other three represent 10% and 7%. The energy contribution of the fourth mode is less than 4%, therefore it can be neglected. Consequently, a 3-mode POD model appears to be a good choice for the flow of Test 3. Figure 27 shows the variation in time of the three respective generalized coordinates. All three generalized coordinates feature significant low frequency components. The responses still look random but at much lower frequencies than in the case of Test 2. It is not clear what physical phenomenon these low frequencies represent.

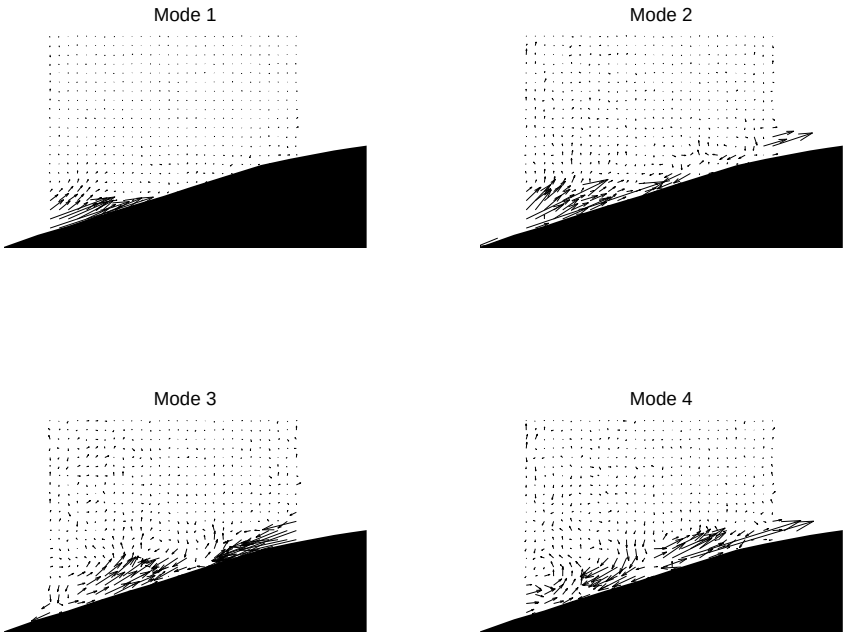

Figure 22: First four modes for Test 1

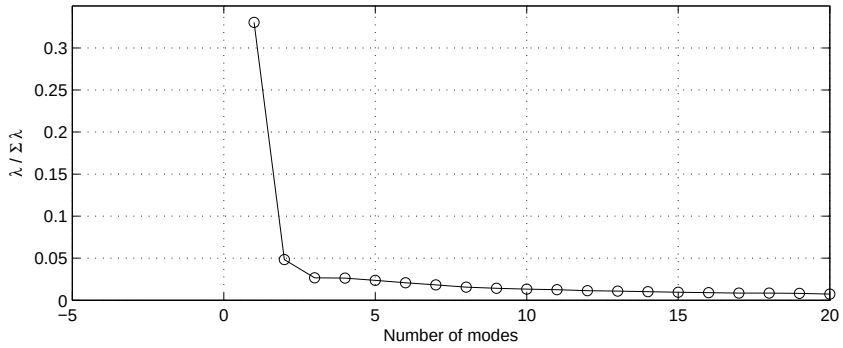

Figure 23: Eigenvalue ratios for the first 20 eigenvalues for Test 1

7 Conclusions

The acquisition and installation of the PIV system for the University of Liege Wind Tunnel facility were successfully conducted. The system has very good capabilities and its performance has been evaluated on two different experiments. All the flow visualizations obtained were reasonable and compatible well with the expected phenomena.

The feasibility of applying Proper Orthogonal Decomposition to the flows visualized using this new system has been demonstrated. This type of decomposition analysis has shown that it can provide some very interesting data about the observed flows, such as dominant mode shapes and frequencies. The analysis has also been performed on flows where the wind tunnel model was vibrating at a significant amplitude. It was shown that this vibration can be detected by the POD procedure using an output-only approach.

In conclusion, the project was very successful and has significantly expanded the

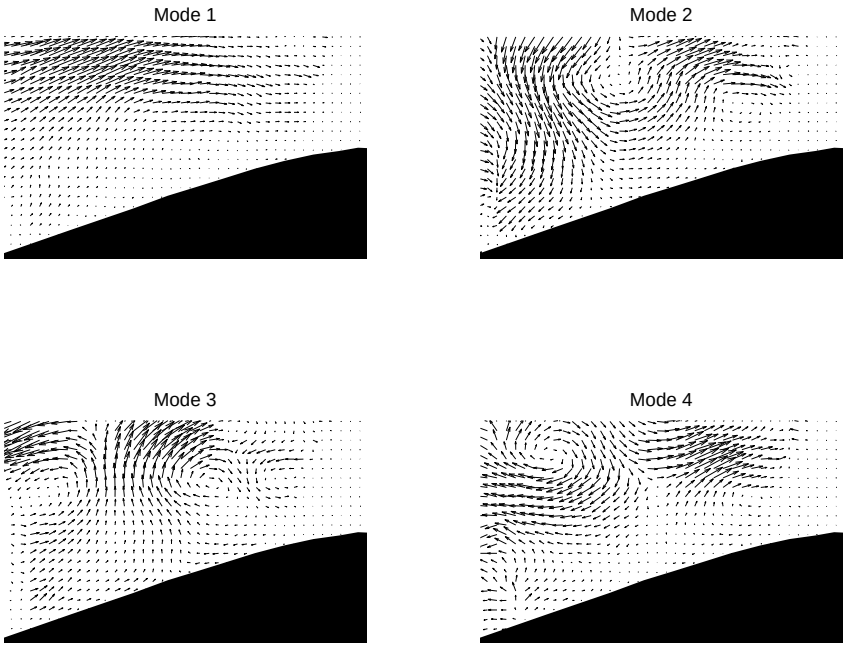

Figure 24: First four modes for Test 2

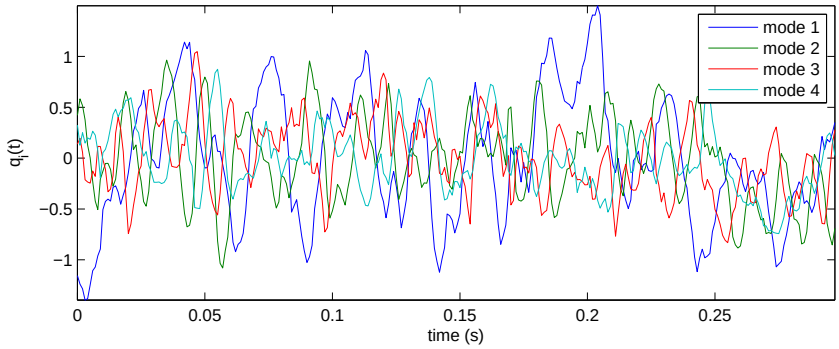

Figure 25: Variation in time of the four retained generalized coordinates, Test 2

capabilities of the ULg Wind Tunnel.

8 Future Work

The limits of the capability of the new PIV system have not been tested yet. It will be of interest to investigate to what extent the system can observe the existence of turbulence, at least in a separated flow. To that end, the influence of several system parameters must be investigated, such as the number of illuminated particles in each shot, the image size, the maximum resolution of the final recovered vector field etc. Some comments about the existence of laminar and turbulent modes have been made in this report but these need to be further substantiated.

All the decompositions described in this work were based on output-only models. However, if the fluid is seen as a system that has its own dynamics but that is also subjected to external excitation in the form of structural vibration, there is scope

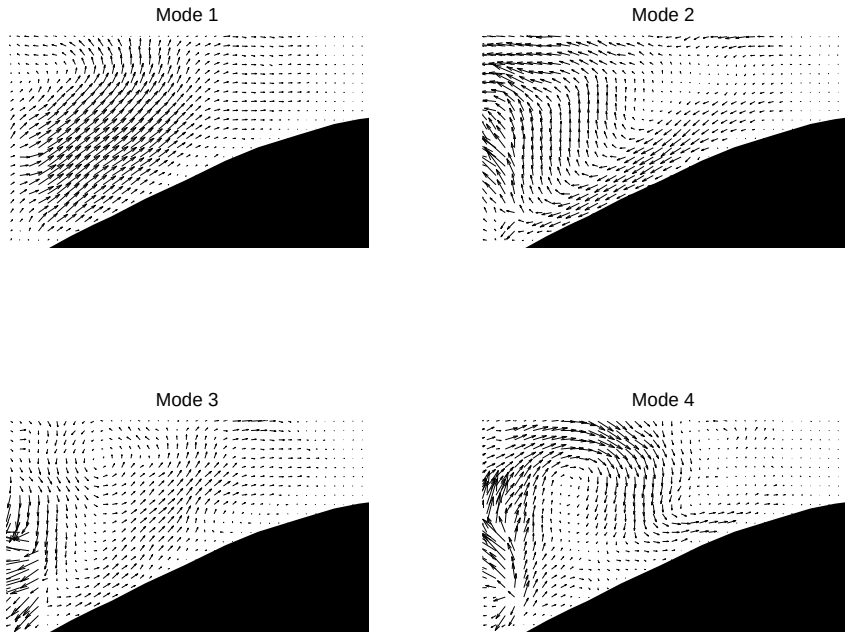

Figure 26: First four modes for Test 3

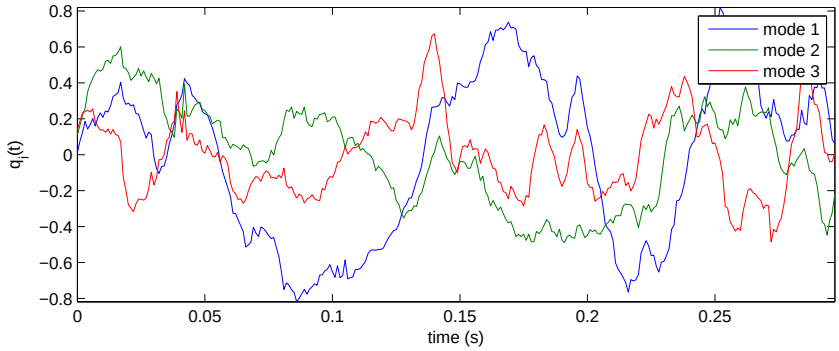

Figure 27: Variation in time of the three retained generalized coordinates, Test 3

for employing input-output modeling methods. Future work will focus on applying subspace methods to the fluid, in a manner similar to the technique used by Tang et al [3]. The excitation will be the measured vibration of the wind tunnel model. Furthermore, the creation of complete aeroelastic models by combining modal tests on the structure with the subspace fluid model will be attempted.

Specifically for the circular cylinder experiment, it would be useful to obtain PIV measurements at many span-wise positions during resonance and to determine whether the flow frequencies are constant throughout the span. It may be possible that lock-in occurs in the outboard sections of the structure, where the vibration amplitude is high, while it does not occur in the inboard sections.

Finally, for the wing experiment, it would be useful to build and test a wing with a smaller chord, so that a bigger section of the flow over its upper surface can be visualized. Such tests will serve to better evaluate the capabilities of POD when applied to flows around wings. Finally, the construction of an oscillating wing is being undertaken, in order to apply decomposition methods to flow around wings

undergoing stall flutter.

References

[1] K. C. Hall. Eigenanalysis of unsteady flows about airfoils, cascades, and wings. *AIAA Journal*, 32(12):2426–2432, 1994.

[2] E. H. Dowell, K. C. Hall, and M. C. Romanowski. Eigenmode analysis in unsteady aerodynamics: Reduced order models. *Applied Mechanics Reviews*, 50(6):371–385, 1998.

[3] D. Tang, D. Kholodar, J.-N. Juang, and E. H. Dowell. System identification and proper orthogonal decomposition method applied to unsteady aerodynamics. *AIAA Journal*, 39(8):1569–1576, 2001.

[4] J. L. Lumley. Atmospheric turbulence and radio wave propagation. pages 116–178. Nauka, Moscow, 1967.

[5] M. Tutkun, P. B. V. Johansson, and W. K. George. Three-component vectorial proper orthogonal decomposition of axisymmetric wake behind a disk. *AIAA Journal*, 46(5):1118–1134, 2008.

[6] K. M. Cipolla, A. Liakopoulos, and D. Rockwell. Quantitative imaging in proper orthogonal decomposition of flow past a delta wing. *AIAA Journal*, 36(7):1247–1255, 1998.

[7] Y. Kim, D. Rockwell, and A. Liakopoulos. Vortex buffeting of aircraft tail: Interpretation via proper orthogonal decomposition. *AIAA Journal*, 43(3):550–559, 2005.

[8] T. Lie and C. Farhat. Adaptation of aeroelastic reduced-order models and application to an F-16 configuration. *AIAA Journal*, 45(6):1244–1257, 2007.